

## A broadband search for coherent emission in radio-cataclysmic variables

MARGARET E. RIDDER <sup>1,2</sup> PAUL E. BARRETT <sup>3</sup> CRAIG O. HEINKE <sup>1</sup> AND GREGORY R. SIVAKOFF <sup>1</sup>

<sup>1</sup>*University of Alberta Physics Dept., CCIS 4-183, Edmonton, AB, T6G 2E1, Canada*

<sup>2</sup>*U.S. Naval Research Laboratory, 4555 Overlook Ave SW, Washington, DC 20375*

<sup>3</sup>*The George Washington University, Corcoran Hall Room 404C, 725 21st St NW, Washington, DC 20052*

### ABSTRACT

Radio observations of cataclysmic variables have revealed a variety of behavior. From some systems, we see bright unpolarized radio flares occurring during dwarf nova outbursts, consistent with synchrotron emission from jets. In others, we see highly polarized emission, restricted in frequency, superimposed on a flat-spectrum continuum, suggesting a coherent emission process. Here, we present spectro-temporal analysis of 2–4 GHz and 8–12 GHz VLA observations of 6 cataclysmic variables. Our results show both broad- and narrow-band, highly polarized, variable radio emission. We suggest that this emission is consistent with electron-cyclotron maser emission or plasma radiation. This could be from an isolated emission region in the case of the narrow-band emission, or a region with varying magnetic field strength or density in the case of the broad-band emission. In one target, V2400 Oph, we see largely unpolarized emission changing on minute timescales, that may coincide with interactions between the white dwarf’s magnetosphere and diamagnetic blobs.

*Keywords:* Cataclysmic variable stars (203) — AM Herculis stars (32) — DQ Herculis stars (407) — Radio continuum emission (1340) — Radio transient sources (2008) — Stellar activity (1580) — M dwarf stars (982)

### 1. INTRODUCTION

The nature of radio emission from cataclysmic variables (CVs) is not yet clear, with evidence for multiple mechanisms, including synchrotron emission from jets (D. L. Coppejans & C. Knigge 2020) and coherent plasma emission processes (G. Chanmugam & G. A. Dulk 1982; P. E. Barrett et al. 2017; P. Barrett et al. 2020; M. E. Ridder et al. 2025). Wideband studies of their radio spectra, polarization, and variability are capable of constraining their radio emission mechanisms. Polarization measurements of a few dozen magnetic CVs suggest a high fractional circular polarization (P. E. Barrett et al. 2017; P. Barrett et al. 2020), but often with large uncertainties. Currently published data on radio polarization of magnetic CVs have generally not tested whether the polarized flux is produced in short-duration flares, in frequency-limited spectral windows, or both. This gap in the literature makes it difficult to ascertain the exact radio emission mechanism responsible in magnetic CVs, aka polars and intermediate polars (IPs).

However, a few magnetic CVs have been shown to exhibit high variability and large fractional polarization. For example, historic observations of AM Her have seen it as bright as  $\sim 10$  mJy with  $\sim 100\%$  circular polarization (G. Chanmugam & G. A. Dulk 1982). Multiple mechanisms have been proposed for the flaring and quiescent emission, including gyrosynchrotron emission (G. Chanmugam & G. A. Dulk 1982) and electron-cyclotron maser emission (ECME; G. A. Dulk et al. 1983). Later observations by P. Barrett et al. (2020) uncovered high degrees of circular polarization in a number of CVs such as MR Ser and ST LMi, although many CVs in their sample did not have sufficient S/N to clearly determine their polarization fraction.

Currently, there are only two confident detections of IPs at radio frequencies in the literature, V1323 Her (P. E. Barrett et al. 2017) and V2400 Oph (M. E. Ridder et al. 2023), but there are over two dozen known detections (P. E. Barrett priv. comm.). V2400 Oph is of particular interest due to its unusual accretion geometry. In normal IPs, matter is accreted from the donor star into an accretion disk around the WD. From there, ionized matter in the

**Table 1.** The list of targets. Coordinates and distances are from *Gaia* EDR3 (C. A. L. Bailer-Jones et al. 2021).

Name	RA (deg)	Dec (deg)	Distance (pc)	Classification
EF Eri	48.555884	-22.595499	160.0 ± 4.0	Polar
UZ For	53.869471	-25.739386	238.0 ± 3.0	Polar
ST LMi	166.415697	25.107827	114.2 ± 0.9	Polar
MR Ser	238.196448	18.941621	131.2 <sup>+0.5</sup> <sub>-0.7</sub>	Polar
V2400 Oph	258.151755	-24.245759	700.0 <sup>+10.0</sup> <sub>-11.0</sub>	IP
V603 Aql	282.227705	0.584085	315.0 <sup>+3.0</sup> <sub>-4.0</sub>	Old nova

evacuated inner disk follows the WD’s magnetic field lines onto the magnetic poles. However, V2400 Oph is thought to be a “diskless” IP that undergoes “diamagnetic blob accretion,” where blobs of material orbit around the WD and then interact with the WD’s magnetic field, either threading onto magnetic field lines to allow accretion, or instead being accelerated and pushed away by the interaction, likely back into the Roche lobe of the donor (A. Langford et al. 2022). Optical photometry revealed multiple features in V2400 Oph’s light curve that could be associated with blobs interacting with the WD or with themselves. For example, low-frequency optical QPOs were attributed to high-energy blobs that migrated outwards, creating a beat frequency between the blob’s orbit and the WD’s spin. Higher-frequency “flickering” might be caused by blobs interacting viscously (A. Langford et al. 2022). Jet production appears to require disk accretion down to small radii (D. Lynden-Bell 1996), so it seems unlikely that such an accretion mechanism would permit a jet.

Thermal free-free emission cannot explain the observed radio emission for many CVs (e.g. G. Chanmugam & G. A. Dulk 1982). Gyrosynchrotron emission may be common among CVs, but at a luminosity too dim to detect at the distances of most CVs with typical current radio observations. Taking QS Vir as an example, its gyrosynchrotron flux density ( $\sim 500 \mu\text{Jy}$ ; M. E. Ridder et al. 2025) if it were placed at 500 pc would be  $5 \mu\text{Jy}$ , which would need several hours on source to detect. The emission detectable at larger distances should be coherent, given that it is intense and, in the cases where polarimetry is available, highly polarized. For example, V2400 Oph is 15 times more radio luminous than the brightest isolated M dwarf stars observed by T. W. H. Yiu et al. (2024). Uncovering what powers V2400 Oph’s radio emission is crucial to understanding the generation of radio emission in CVs, as well as our understanding of coherent plasma emission processes in flare stars by examining a CV’s fast-rotating donor.

In this paper, we present the results from spectral, polarization, and variability analyses on a VLA sample of mostly magnetic CVs in X and S bands, with prior radio observations reported by P. Barrett et al. (2020): the polars MR Ser, ST LMi, UZ For, and EF Eri, the IP V2400 Oph, and the old nova V603 Aql (also studied by D. L. Coppejans et al. 2015).

The frequency of emission in ECME probes the magnetic field strength of the emission region and constrains its location within binaries. The *S*- and *X*-band observations of these CVs probe regions where the magnetic field would be several kG (assuming the emission is at the fundamental frequency), which may include the lower corona of the donor star (G. A. Dulk 1985). An interesting prospect is the possibility of a flux tube connecting the donor and WD in a similar manner to the Jupiter-Io system. A gradually varying magnetic field strength would result multiple fundamental frequencies of emission in the case of ECME and could result in a broad-spectrum, highly polarized signal.

## 2. OBSERVATIONS AND ANALYSIS

Table 1 gives positions and distances of the 6 CVs studied in this work using the Jansky Very Large Array (VLA). They were each observed twice in *X*-band (8–12 GHz) in 1-hour blocks (PI Barrett; ObsIDs 17B-144, 19A-166). All but one source, V603 Aql, were also observed in *S*-band (2–4 GHz; PI Ridder, ObsID 25A-404).

Parallel-hand calibration, as well as automatic and manual flagging, was conducted with the Common Astronomy Software Applications (CASA; CASA Team et al. 2022) pipeline version 6.5.4. We did not perform self-calibration on these observations. A summary of the primary (flux/bandpass/polarization angle) calibrators and secondary (complex gain) calibrators is given in Table 2, including leakage calibrators for the *S*-band observations. Leakage calibration was not conducted as part of the *X*-band observations. While this raises the noise for Stokes V *X*-band measurements, the leakage moduli for the VLA have been shown to be around 5% (C. A. Hales 2017). We assume this value as a lower limit to our  $1\sigma$  uncertainty for *X*-band Stokes V in Table 3.

**Table 2.** The list of primary, secondary, and (for S) leakage calibrators, and VLA configurations, used for each source.

Name	Primary	Secondary	VLA Config	Primary	Secondary	Leakage	VLA Config
	X (8-12 GHz)			S (2-4 GHz)			
EF Eri	3C138	J0329–2357	B	3C138	J0240-2309	J0319+4130	D
UZ For	3C138	J0329–2357	B	3C138	J0416-1851	J0319+4130	D
ST LMi	3C286	J1125+2610	B	3C286	J1125+2610	J1407+2827	D
MR Ser	3C286	J1520+2016	B	3C286	J1553+1256	J1407+2827	D
V2400 Oph	3C286	J1744–3116	B	3C286	J1751-2524	J1407+2827	C
V603 Aql	3C286	J1856+0610	B	...	...	...	...

**Table 3.** The  $X$ -band (8–12 GHz) flux in Stokes I and Stokes V for each target in our sample. Stokes V fluxes were produced by a forced fit at the Stokes I position. We impose a lower limit on the polarization fraction uncertainty of 5% due to the absence of a leakage calibrator. Sources where the uncertainty was raised to this level are marked with an asterisk. The polarization handedness is denoted either left-circularly polarized (LCP) for negative values of Stokes V or right-circularly polarized (RCP) for positive values, following the IAU convention.

Name	Date	Stokes I flux ( $\mu$ Jy)	Stokes V flux ( $\mu$ Jy)	Pol. fraction (%)
EF Eri	2017 September 28	$157 \pm 6$	$-124 \pm 6$	$79 \pm 5$ LCP
EF Eri	2017 October 2	$67 \pm 5$	$-48 \pm 5$	$71 \pm 9$ LCP
UZ For	2017 October 17	$30 \pm 5$	$-5 \pm 5$	$17 \pm 17$ LCP
UZ For	2017 October 19	$35 \pm 5$	$13 \pm 5$	$37 \pm 15$ RCP
ST LMi	2017 November 1	$80 \pm 5$	$-8 \pm 5$	$10 \pm 6$ LCP
ST LMi	2017 November 5	$40 \pm 5$	$-11 \pm 5$	$28 \pm 13$ LCP
MR Ser	2017 October 11	$42 \pm 6$	$4 \pm 6$	$10 \pm 14$ RCP
MR Ser	2017 November 25	$308 \pm 8$	$256 \pm 8$	$83 \pm 5^*$ RCP
V2400 Oph	2019 April 25	$266 \pm 8$	$-10 \pm 8$	$4 \pm 5^*$ LCP
V2400 Oph	2019 May 11	$320 \pm 8$	$2 \pm 3$	$0 \pm 5^*$ RCP
V603 Aql	2017 December 18	$90 \pm 10$	$30 \pm 10$	$33 \pm 12$ RCP
V603 Aql	2018 January 25	$71 \pm 7$	$2 \pm 6$	$2 \pm 8$ RCP

2–4 GHz and 8–12 GHz images in Stokes I, Q, U, and V were produced by WSClean (A. R. Offringa et al. 2014). In addition to imaging the full band, we also produced images with the bandwidth of a VLA spectral window (128 MHz). Each target scan from the observations was split into roughly 10 time bins to produce light curves and dynamic SEDs (shown in the next section), to search for variable emission features and potential flares.

Assuming each target was a point source, each was fit with a 2D Gaussian using their *Gaia* EDR3 positions (C. A. L. Bailer-Jones et al. 2021). The peak intensity normalization and source position were left as free parameters in the full-band Stokes I images. This position was fixed for full band Stokes V images and all other images produced for the SEDs and light curves, while leaving the peak intensity normalization free.

### 3. RESULTS

The Stokes I and Stokes V fluxes as well as circular polarization fractions in  $X$ - and  $S$ -band are shown in Tables 3 and 5, respectively. MR Ser, ST LMi, and V2400 Oph were detected at 2–4 GHz in Stokes I and (except for one observation of V2400 Oph) in Stokes V. All sources in our sample were detected at 8–12 GHz in Stokes I, but only EF Eri, MR Ser, and V603 Aql were detected in Stokes V at  $\geq 3\sigma$ . No sources were detected in Stokes Q and U. The full-band SEDs, light curves, and dynamic SEDs are presented in Figs. 1 to 10. Alternative, 2-dimensional versions of the 1-dimensional dynamic SEDs therein are available in an online repository<sup>4</sup>. Uncertainties presented in this section are the RMS of a background region, defined as an annulus with  $35\text{--}100\times$  the area of a circle with the same radius as

<sup>4</sup> <https://doi.org/10.5281/zenodo.18460656>

**Table 4.** The X-band (8–12 GHz)  $3\times$ RMS upper limits on linear polarization.

Name	Date	Lin. pol. flux ( $\mu$ Jy)	Pol. fraction (%)
EF Eri	2017 September 28	<23	<15
EF Eri	2017 October 2	<22	<33
UZ For	2017 October 17	<24	<80
UZ For	2017 October 19	<22	<63
ST LMi	2017 November 1	<21	<26
ST LMi	2017 November 5	<21	<53
MR Ser	2017 October 11	<25	<60
MR Ser	2017 November 25	<26	<8
V2400 Oph	2019 April 25	<34	<13
V2400 Oph	2019 May 11	<37	<12
V603 Aql	2017 December 18	<39	<43
V603 Aql	2018 January 25	<27	<38

**Table 5.** The S-band (2–4 GHz) fluxes in Stokes I and Stokes V for each target in our sample. Upper limits on the Stokes I and V fluxes for EF Eri and UZ for are equal to  $3\times$ RMS. The absolute value of the polarization fraction is quoted for these targets because there is no directionality in the error estimates.

Name	Date	Stokes I flux ( $\mu$ Jy)	Stokes V flux ( $\mu$ Jy)	Pol. fraction (%)
EF Eri	2025 March 19	<100	<  26	<  26
UZ For	2025 March 22	<39	<  21	<  54
ST LMi	2025 March 23	$160 \pm 25$	$-87 \pm 6$	$54 \pm 9$ LCP
MR Ser	2025 April 5	$87 \pm 16$	$59 \pm 5$	$67 \pm 14$ RCP
V2400 Oph	2025 August 9	$519 \pm 15$	$1 \pm 6$	–
V2400 Oph	2025 August 15	$637 \pm 15$	$247 \pm 7$	$39 \pm 1$ RCP

**Table 6.** The S-band (2–4 GHz)  $3\times$ RMS upper limits on linear polarization.

Name	Date	Lin. pol. flux ( $\mu$ Jy)	Pol. fraction (%)
EF Eri	2025 March 19	<61	<61
UZ For	2025 March 22	<30	<77
ST LMi	2025 March 23	<30	<19
MR Ser	2025 April 5	<31	< 36
V2400 Oph	2025 August 9	<28	<5
V2400 Oph	2025 August 15	<28	<4

the beam major axis (depending on how crowded the field). The inner radius of this annulus was equal to the beam major axis.

### 3.1. *EF Eri*

EF Eri was detected in both epochs in Stokes I and Stokes V. Two minute-scale flares (see Fig. 1) were detected, one in each epoch, each corresponding to an increase in circular polarization. At the peak of the flares, the polarization fraction was  $96 \pm 5\%$  LCP on 2017 September 28 and  $79 \pm 5\%$  LCP on 2017 October 2. In the corresponding dynamic SEDs, a broadband spectral feature appears at the peak of both flares, which has a slightly negative fit to the spectral index in the first observation ( $\alpha = -0.7 \pm 0.2$ ), and a somewhat positive index in the second ( $\alpha = 2.7 \pm 0.8$ ).

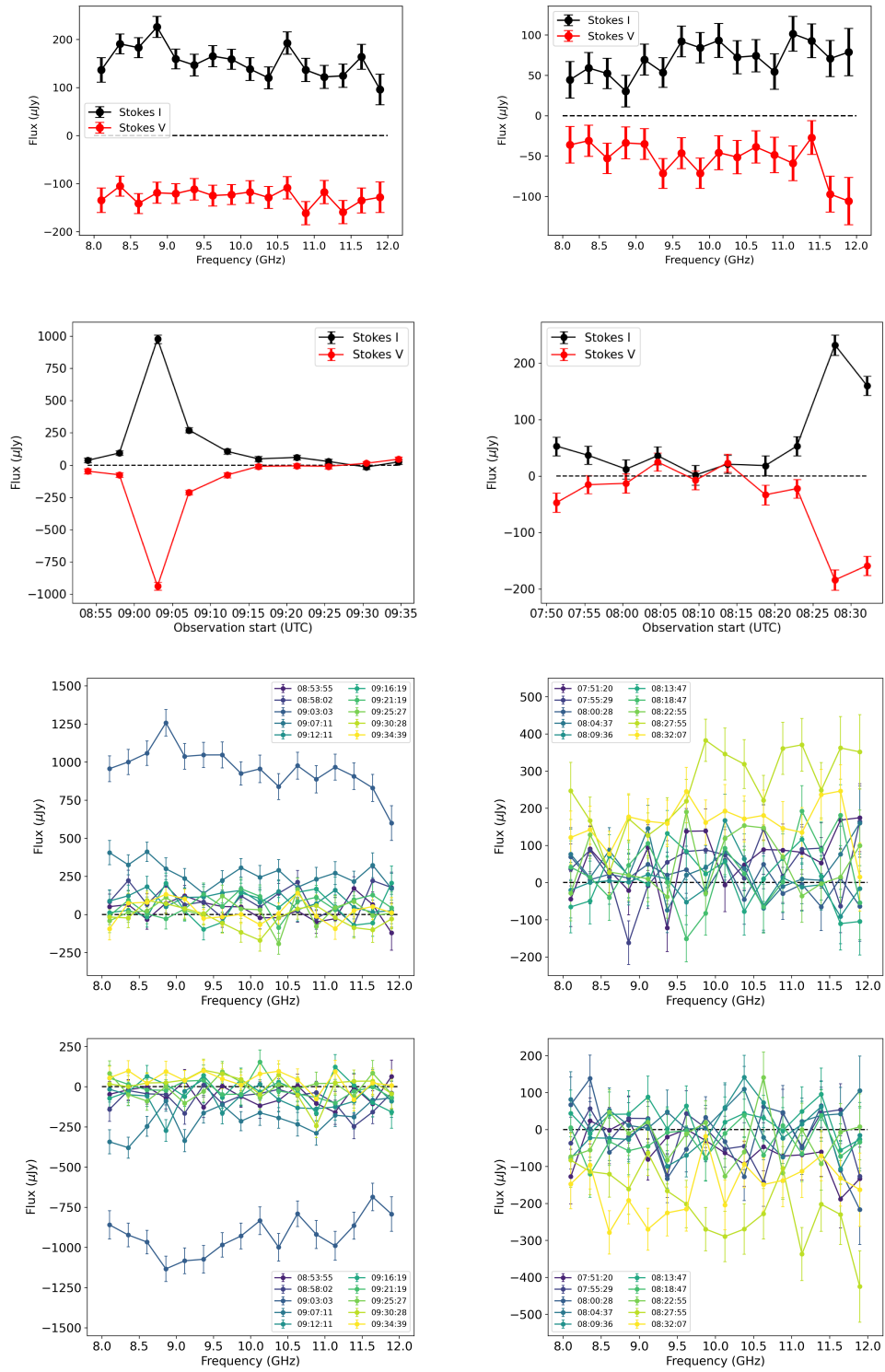


**Figure 1.** The 8–12 GHz data for EF Eri on 2017 September 28 (*left column*) and 2017 October 2 (*right column*). The top panels show the full-band SEDs, the second panels show the full-band light curves, the third panels show the Stokes I dynamic SEDs, and the bottom panels show the Stokes V dynamic SEDs. One flare was detected in each 8–12 GHz observation of EF Eri. Both produced broadband LCP emission.

EF Eri was not detected in the 2–4 GHz observations on 2025 March 19. The  $3\times$ RMS upper limit on this observation,  $96 \mu\text{Jy}$ , is consistent with the quiescent emission (that which is outside the flare) observed at 8–12 GHz.

### 3.2. UZ For

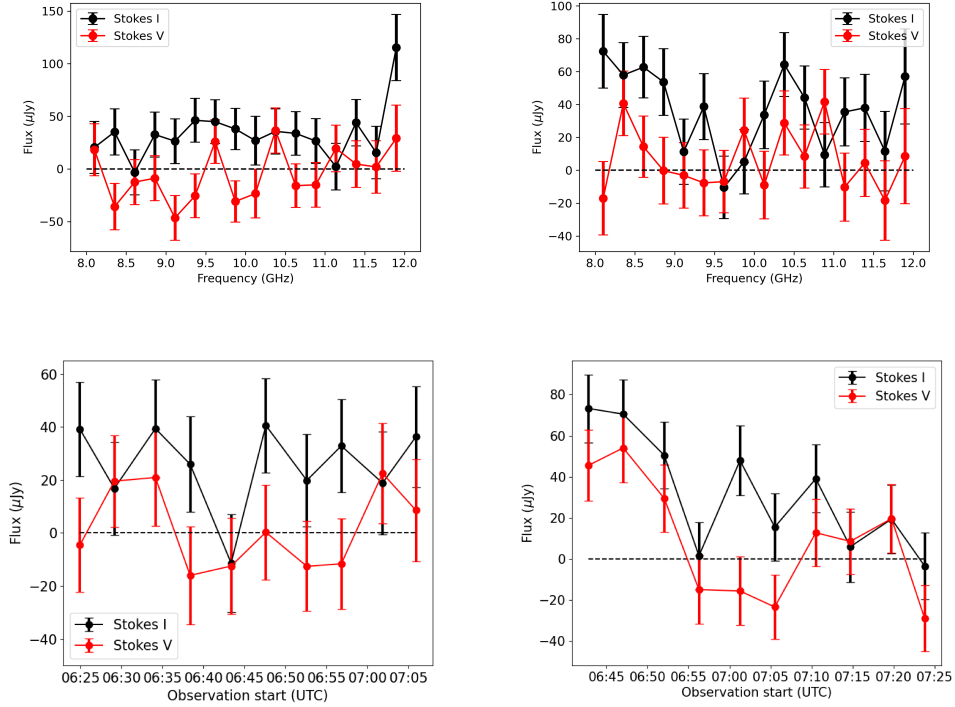


**Figure 2.** The 8–12 GHz data of UZ For on 2017 October 17 (*left column*) and 2017 October 19 (*right column*). The top panel shows the full-band SEDs, while the bottom panel shows the full-band light curves. There are neither clear flares nor circular polarization detected.

While UZ For, the only eclipsing system in our sample, was detected in both epochs in Stokes I, it was undetected in Stokes V, and there are no obvious emission features in either SED (Fig. 2). The light curve for 2017 October 19, suggests some amount of variation that corresponds with increasing circular polarization, but the measurement is marginal. Averaging over the first three and the following three data points, UZ For decreases in flux by about a factor of 2. This fractional change is similar to what was observed in QS Vir during previous observations (M. E. Ridder et al. 2025). The S/N is unfortunately too low for further analysis, including the examination of its dynamic SEDs.

UZ For was not detected in the 2–4 GHz observations on 2025 March 22.

### 3.3. ST LMi

Most of the data on ST LMi lack clear signals of variation or circular polarization, but near the end of the first observation (Fig. 3), there is an increase suggestive of a flare, with a significant increase in circular polarization. Over the last 15 minutes of the observation, the fractional polarization is  $38 \pm 12\%$  LCP. Due to the relatively low S/N ratio, we do not present 8–12 GHz dynamic SEDs for ST LMi.

At 2–4 GHz, ST LMi appears to have a flat spectrum with a large fractional polarization (Fig. 4). The origin of the polarized flux seems to be two bright flares at early and late times during the observation. The only two clear detections in Stokes I with acceptable uncertainties are in the first and final time bins, which suggest a broadband signal. These features are much clearer in the Stokes V dynamic SED, which shows that these flares produced large fractional LCP.

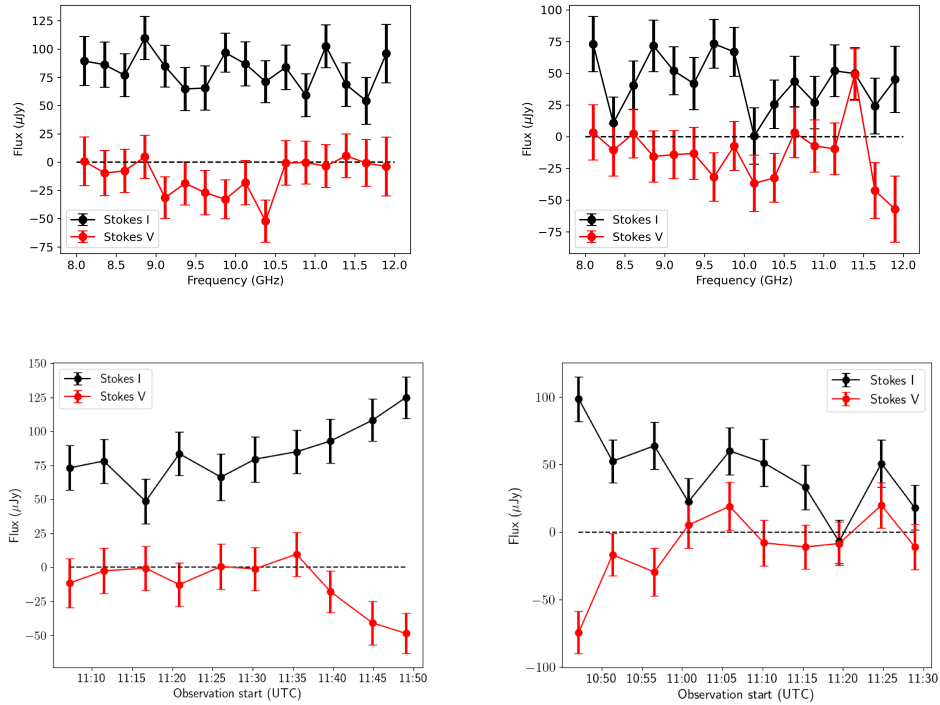


**Figure 3.** The 8–12 GHz data for ST LMi on 2017 November 1 (*left column*) and 2017 November 5 (*right column*). The top panels show the full-band SEDs, while the bottom panels show the full-band light curves. Detections of circular polarization are marginal, but there is an indication of increasing polarization with flux at the end of the first observation and the beginning of the first.

### 3.4. MR Ser

In the first observation of MR Ser on 2017 October 11 (Fig. 5), there was no clear Stokes V detection, no variation, and no emission features in the SED. However, on 2017 November 25, there is a strong flare (factor of  $\sim 18$ ) that peaks at 21:47 UTC. We only observe the rise of the flare, lasting  $\sim 10$  minutes. This flare corresponds with a broadband emission feature that then becomes more localized near 10–10.5 GHz before it begins to decay. At the peak, it is  $90 \pm 5\%$  RCP.

The behavior at 2–4 GHz is somewhat different by comparison. Stokes V is indeed detected (Fig. 6) and there is a flare at 17:30 UTC on 2025 April 5, but the spectral shape of the flare is difficult to determine in the Stokes I dynamic SED. This may be due to the crowded nature of the field raising the background noise in each time bin. If we assume that Stokes V is representative of the shape of the spectrum, the circularly polarized flare from MR Ser in *S*-band is narrow-band, centered on 2.4 GHz with a FWHM of  $\sim 0.5$  GHz.

### 3.5. V2400 Oph

V2400 Oph was detected in Stokes I in both epochs of *X*-band observations, but was undetected in Stokes V. Using a power law fit, assuming  $S \propto \nu^\alpha$ , we fit the SEDs to calculate the spectral index. Over the whole frequency band, the spectral index was  $-2.5 \pm 0.3$  on 2019 April 25 and  $-2.2 \pm 0.2$  on 2019 May 11. Despite some small variations (Fig. 7, it remained spectrally steep throughout the first observation. During the second observation, however, there is statistically significant variation in the spectral index (Fig. 8). At the point where V2400 Oph was brightest, the spectrum became almost flat and as it dimmed, the index dramatically steepened to  $\sim -4$ . We searched for linear polarization, but found no source at the Stokes I position in Stokes Q or U.

On 2025 August 9, V2400 Oph was detected in Stokes I, but undetected in Stokes V, at 2-4 GHz. On 2025 August 15, it was detected in both Stokes I and Stokes V at 2-4 GHz (Fig. 9). The light curves appear to show a slow variation similar to the 8–12 GHz data, but also show bright, rapid flaring that is sometimes polarized.

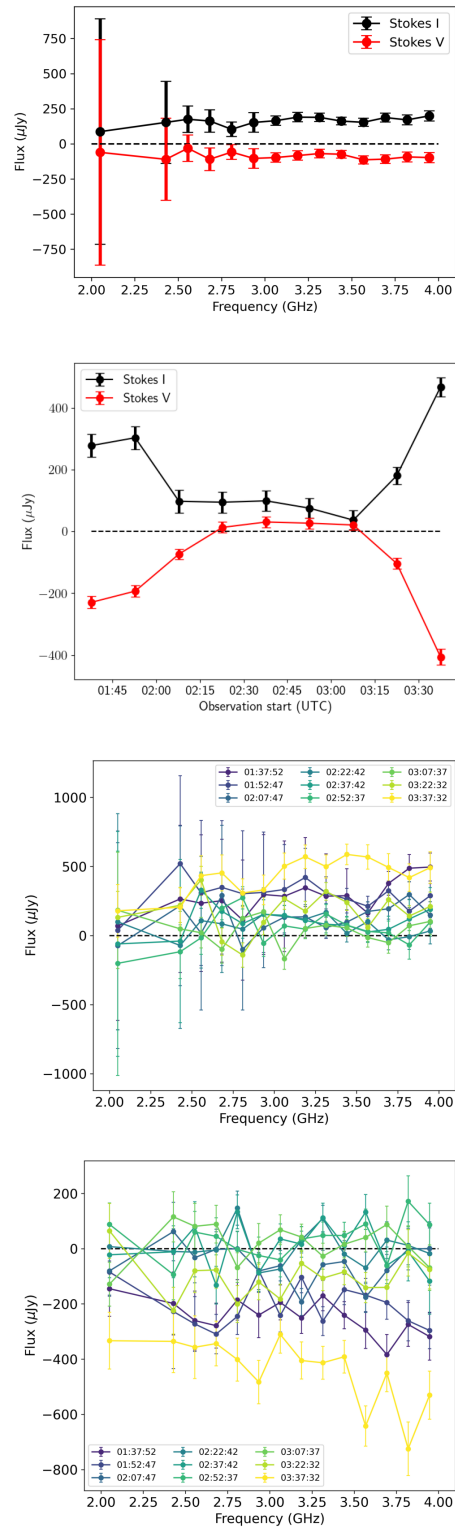


**Figure 4.** The 2–4 GHz data for ST LMi on 2025 March 23. The top panel shows the full-band SED, the second panel shows the full-band light curve, the third panel shows the Stokes I dynamic SED, and the bottom panel shows the Stokes V dynamic SED. There are two flares detected at the beginning and end of the observation that correspond with clear detections of LCP emission.

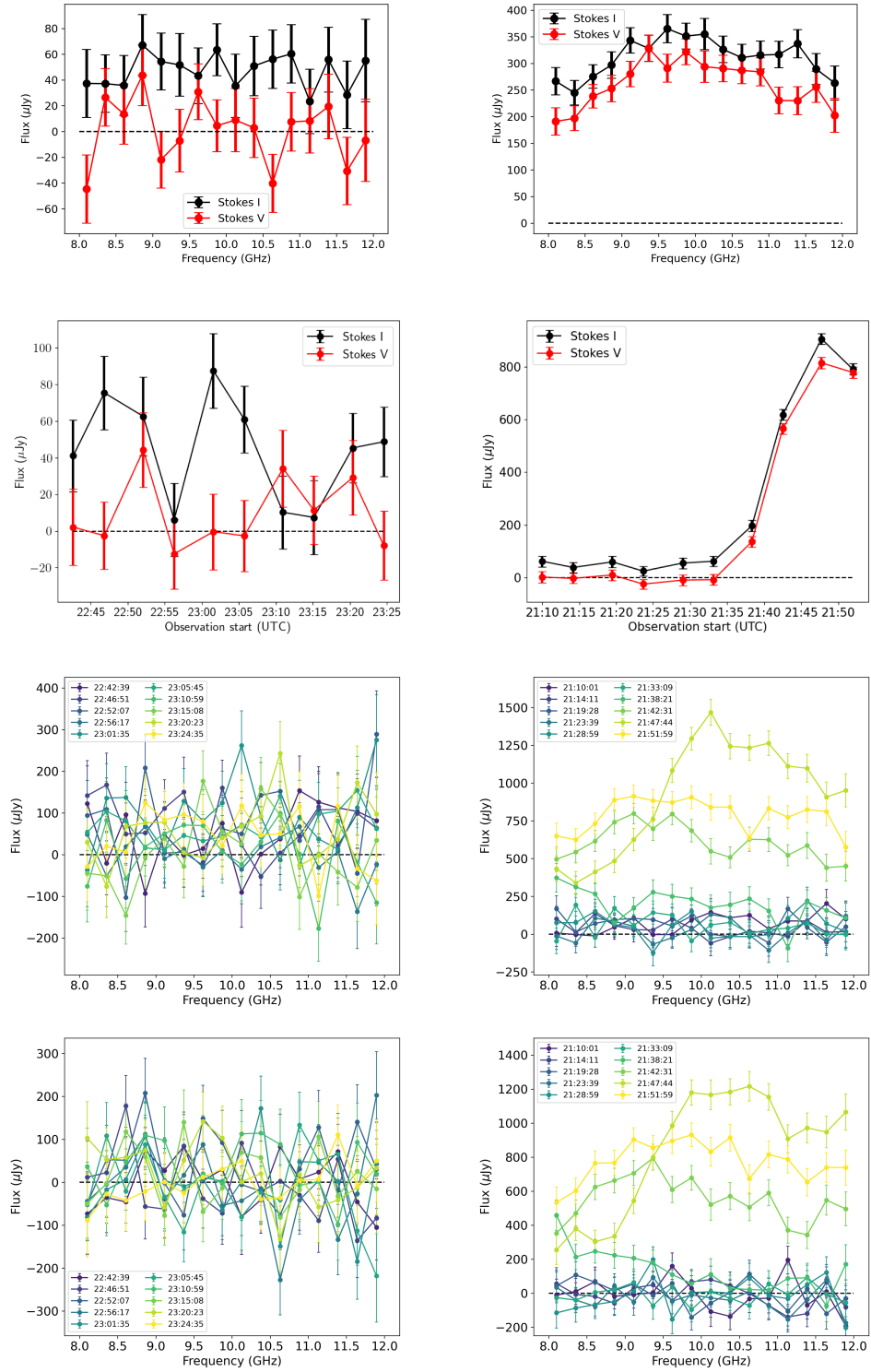


**Figure 5.** The 8–12 GHz data for MR Ser on 2017 October 11 (*left column*) and 2017 November 25 (*right column*). The top panels show the full-band SEDs, the second panels show the full-band light curves, the third panels show the Stokes I dynamic SEDs, and the bottom panels show the Stokes V dynamic SEDs. One flare was detection in the second observation, which was highly circularly polarized.

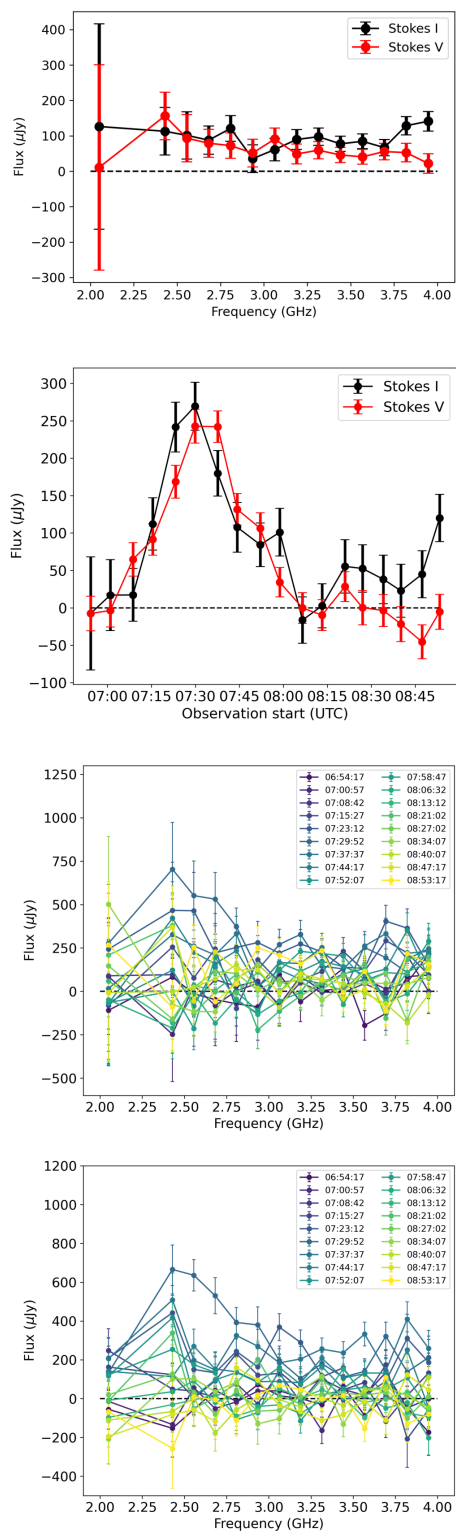


**Figure 6.** The 2–4 GHz data for MR Ser on 2025 April 5. The top panel shows the full-band SED, the second panel shows the full-band light curve, the third panel shows the Stokes I dynamic SED, and the bottom panel shows the Stokes V dynamic SED. One flare was detected in this observation. It is difficult to see any clear signal in the Stokes I data, but the shape is somewhat clearer in Stokes V.

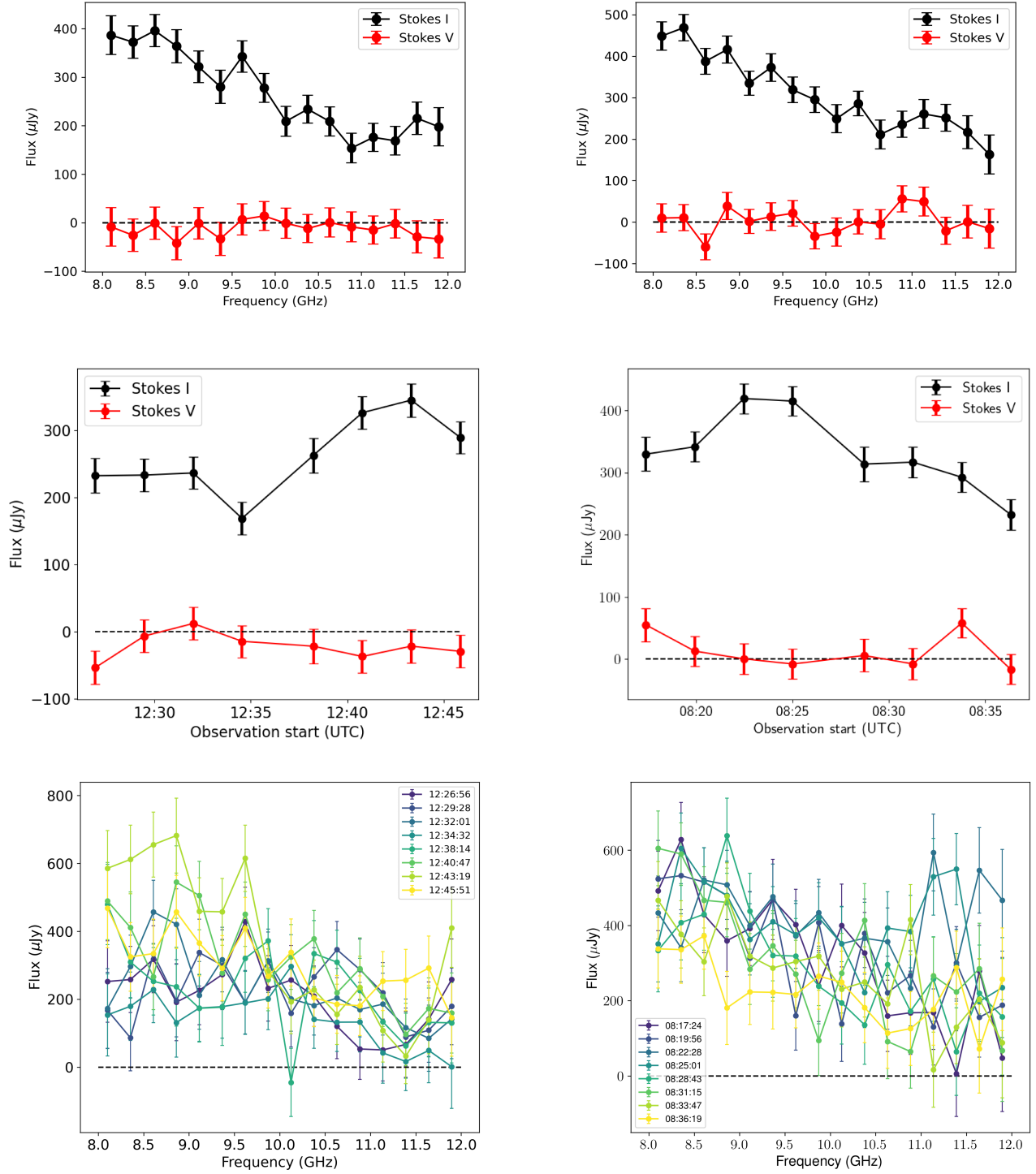


**Figure 7.** The 2–4 GHz data for V2400 Oph on 2019 April 25 (*left column*) and 2019 May 11 (*right column*). The top panels show the full-band SEDs, the middle panels show the full-band light curves, and the bottom panels show the dynamic SEDs in Stokes I. There is some moderate variation in each observation, but no obvious flares were detected.

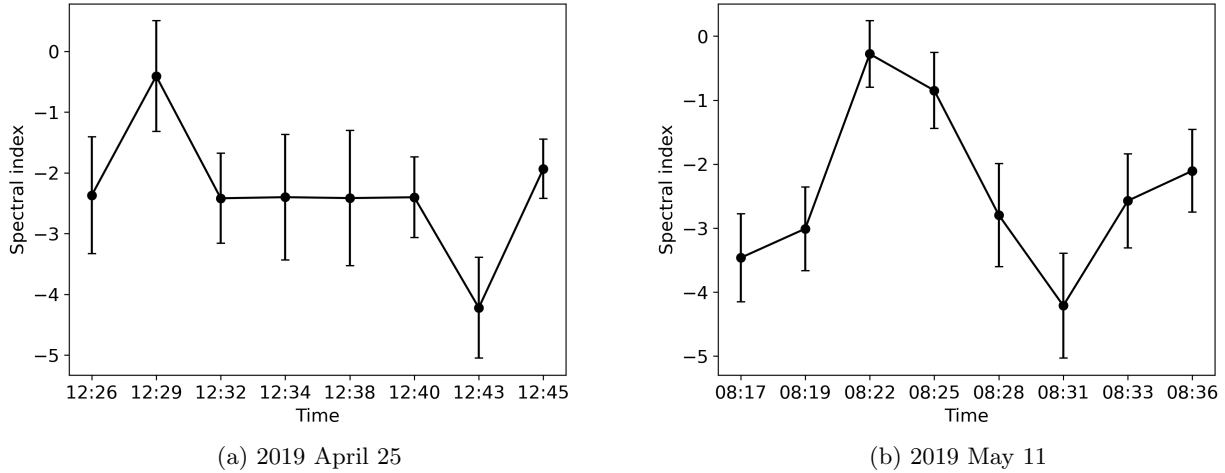


**Figure 8.** The spectral index of V2400 Oph on 2019 April 25 and 2019 May 11, produced by fits of a power law to the X-band dynamic SEDs in Fig. 7. In the first epoch (*left*), the spectral index is mostly stable, but in the second epoch (*right*), there is a clear evolution from flat to steep over  $\sim 6$  minutes.

**Table 7.** The non-flaring flux ranges for all targets except for V2400 Oph. For observations of EF Eri and MR Ser that captured a flare, the 8–12 GHz fluxes surrounding the flare were used to calculate the mean flux. We present the fluxes alongside some relevant binary system parameters that may affect the radio emission (e.g. accretion rate). Some accretion rates were excluded if the literature did not have an estimate that corresponded with the accretion state of each target when the radio observations were taken. To the knowledge of the author, there is currently no spectral type model for V603 Aql. References for the final column are as follows: [1] K. Beuermann et al. (2000), [2] K. Beuermann et al. (2007), [3] L. Ferrario et al. (1993), [4] Z. N. Khangale et al. (2020), [5] T. Rousseau et al. (1996), [6] H. Ritter & U. Kolb (2003), [7] M. R. Sanad & M. Bobrowsky (2015), [8] A. D. Schwope et al. (1993), [9] E. M. Sion et al. (2015), [10] V. F. Suleymanov (1992).

Name	$P_{\text{orb}}$	Flux	Luminosity	WD $ \vec{B} $	$\dot{M}$	Donor	Refs.
	(hr)	( $\mu\text{Jy}$ )	( $\text{erg/s/cm}^2$ )	(MG)	( $M_{\odot}/\text{yr}$ )		
EF Eri	1.35	29–48	8.9–15	44	$3 \times 10^{-11}$	L4–5	[6], [1], [2]
UZ For	2.11	30–35	20–24	57	–	M4.5/5	[5], [6], [4]
ST LMi	1.90	40–80	6.2–12	12	$(6\text{--}200) \times 10^{-14}$	M6/5	[6], [7], [3]
MR Ser	1.89	42–50	6.4–7.6	27	–	M8/5	[6], [8]
V603 Aql	3.32	71–90	84–110	$\sim 5$	$\sim 2 \times 10^{-9}$	–	[6], [9], [10]

### 3.6. V603 Aql

Stokes V flux was only detected in the first epoch of X-band observations for V603 Aql. While there is some variation in the SED (Fig. 10), there is a slight tendency for it to be right circularly polarized. However, there are no clear emission features that could help identify the emission mechanism in either observation. The light curves hint at a decrease in overall flux, but an increase in fractional circular polarization near the end of each observation. The highest Stokes V flux points are higher than the simultaneous Stokes I fluxes, which is impossible. However, because the simultaneous Stokes I and V fluxes are consistent with each other within their uncertainties, we can conclude that they are consistent with 100% RCP at this time in the observation, but not significantly above zero (the errors are 50% and 90% for the first and second observation, respectively).

## 4. DISCUSSION

There is a wide variation in the radio emission from this sample of CVs. Notably, we saw three bright, highly circularly polarized flares from EF Eri and MR Ser at 8–12 GHz. At 2–4 GHz, we observed one circularly polarized

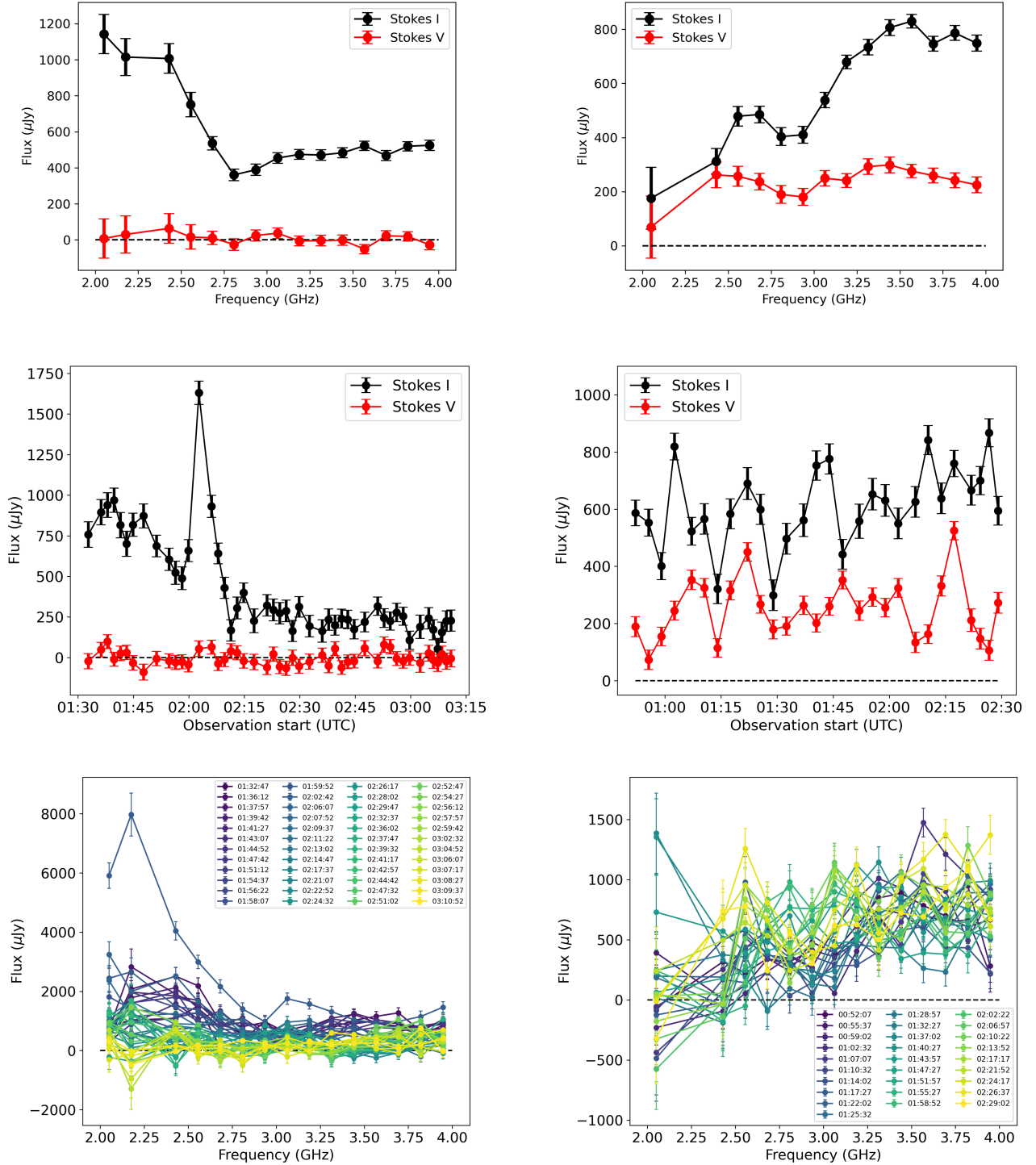


**Figure 9.** The 2–4 GHz data for V2400 Oph on 2025 August 9 (*left column*) and 2025 August 15 (*right column*). The top panels show the full-band SEDs, the middle panels show the full-band light curves, and the bottom panels show the dynamic SEDs in Stokes I. Each observation shows distinct behavior in V2400 Oph: at times emission can be unpolarized, but at others it can be moderately to highly circularly polarized.

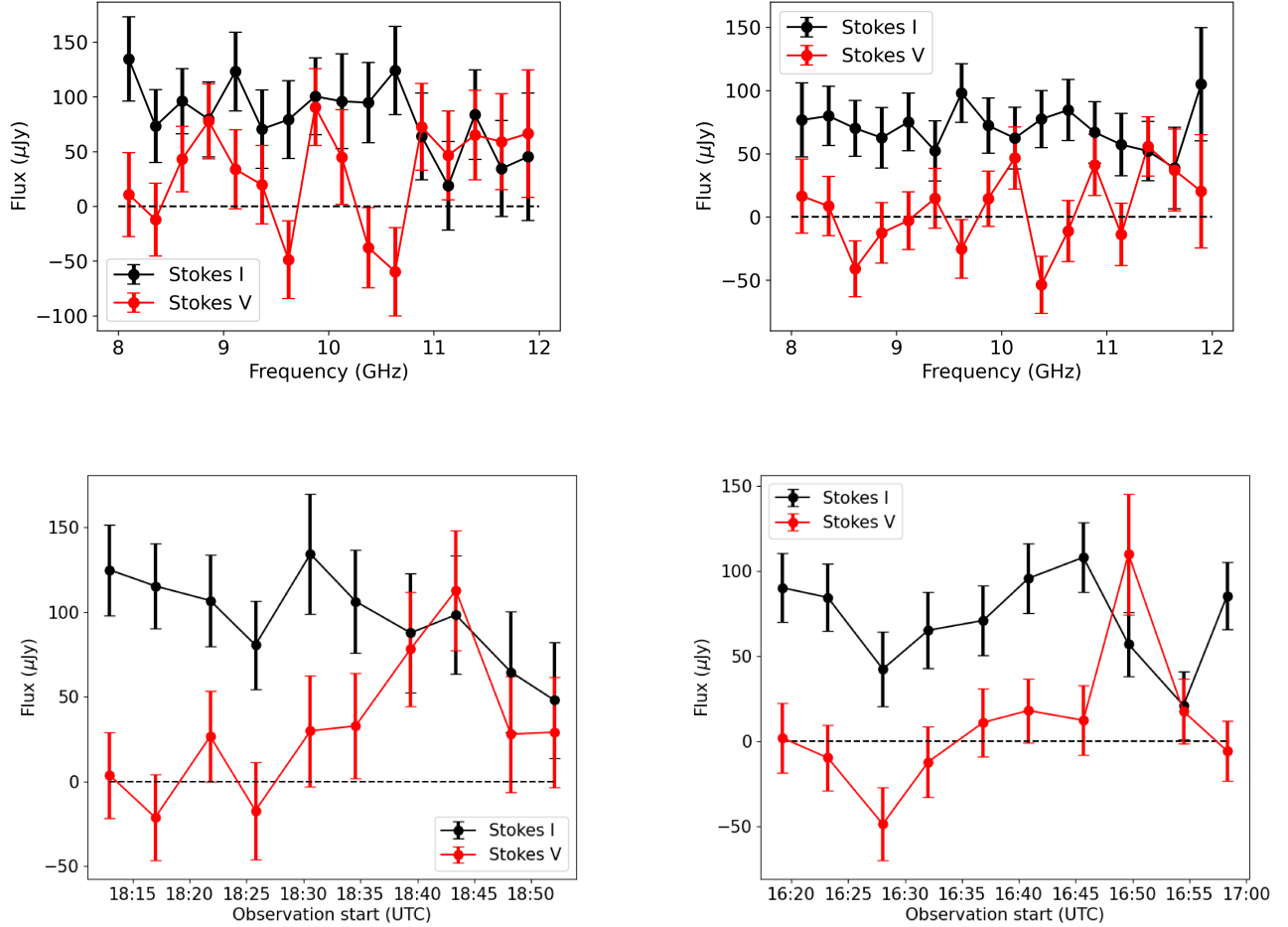


**Figure 10.** The 8–12 GHz data for V603 Aql on 2017 December 18 (*left column*) and 2018 January 25 (*right column*). The top panels show the full-band SEDs, while the bottom panels show the full-band light curves. There are no clear flares, but the light curves show slight variation.

flare from MR Ser, 2 polarized flares from ST LMi, as well as 2 unpolarized flares and rapidly varying polarized emission from V2400 Oph. We have also seen faint, highly circularly polarized candidate flares from UZ For and ST LMi at 8–12 GHz.

The polarization fractions at the peaks of the  $X$ -band flares from EF Eri and MR Ser ranged from 79–96%, which suggests that a coherent emission process is involved, similar to that observed in  $S$ -band observations of QS Vir [M. E. Ridder et al. \(2025\)](#). The peak emission frequency for MR Ser ( $\sim 10$  GHz) corresponds to a magnetic field strength of a few kG, appropriate for an M dwarf star similar to the donor star. ECME is typically restricted in frequency in the non-relativistic limit, so the broadband nature of the emission (see Figs. 1 and 5) seems to argue against ECME as the origin of the radio emission. However, if there were multiple emission regions, each with a different magnetic field strength (e.g. along a flux tube), covering a range of several kG, ECME could reproduce the spectral behavior seen in the SEDs shown above. Unlike in the Jupiter-Io system, the motion powering the flux tube in a CV with a tidally locked donor would need to be the spin of the WD. In polar systems, the WD’s spin is synchronized to the orbital period, making this scenario unlikely for most of our targets. Because the frequency of emission and the bandwidth are similar, we should consider the possibility that plasma radiation is responsible. This too should generate high fractions of circular polarization, but unlike weakly relativistic ECME, can be broadband, and the duration should be less than an hour [J. R. Callingham et al. \(2024\)](#).

Assuming all the above flares are coherent (as indicated by the circular polarization fraction), here we estimate an upper limit on the size of the emission region in the case of incoherent emission. Using the form presented in [H. K. Vedantham \(2021\)](#), the brightness temperature is,

$$T_b = \frac{Fc^2d^2}{2k_B\nu^2\pi R^2}, \quad (1)$$

where  $F$  is the flux density,  $d$  is the distance to the object,  $k_B$  is Boltzmann's constant, and  $R$  is the size of the emitting region. We will assume that the brightness temperature for each flare is  $\gtrsim 10^{12}$  K since this is an approximate transition from incoherent to coherent emission. For EF Eri on 2017 September 28,  $R \leq 5 \times 10^9$  cm, and for 2017 October 2,  $R \leq 2 \times 10^9$  cm. For MR Ser on 2017 November 5,  $R \leq 4 \times 10^9$  cm. For ST LMi on 2025 March 23, the first flare corresponds to  $R \leq 7 \times 10^9$  cm and the second flare corresponds to  $R \leq 8 \times 10^9$  cm. Assuming that the size of a typical M dwarf is  $\sim 10^{10}$  cm, all of the flares we detected must be produced in regions that are less than the size of the donor star, ranging from about 1/5 to 4/5. Note that this does not rule out a region of similar size in between the WD and the donor star or near the WD itself.

The behavior of V4200 Oph is perhaps more difficult to explain. The steep spectral shape and low circular polarization in  $X$ -band (Fig. 7) and  $S$ -band on 2025 August 9 (Fig. 9) would suggest synchrotron emission, which could be produced by a jet launched by the WD in a similar way to SS Cyg [D. L. Coppejans & C. Knigge \(2020\)](#). Although we did not detect any linear polarization in any frequency band, this is not strong evidence against synchrotron emission. The steep spectral indices, however, indicate an optically thin synchrotron emission region, arguing against a compact jet. Another argument against a compact jet is the accretion geometry in V2400 Oph, which is hypothesized to undergo diamagnetic blob accretion, in which small blobs of material are accreted in short bursts [A. Langford et al. \(2022\)](#). We hypothesize that the electron population is accelerated at the interaction site with the WD's rotating magnetic field, leading to the production of synchrotron radiation. Optical observations conducted by the Kepler K2 mission ([A. Langford et al. 2022](#)) show stochastic variation on the scale of  $<1$  ks that has been attributed to interaction between blobs and the WD's magnetic field. We also see variations in the V2400 Oph VLA observations on timescales of  $\sim 300$  seconds (Figs. 7). The evolution of the spectral index on 2019 May 11 may be explained by an initially energetic electron population that emits at higher frequencies, resulting in a flatter spectrum. At later times, the spectrum would steepen as the higher-energy electrons lose energy. This argument should not be taken as definitive, since the lowest spectral index of  $-4$  corresponds to a physically implausible electron population spectral index of  $-10$ .

In diamagnetic blob accretion, blobs that gain enough energy from the WD's magnetic field may be flung out of the system, or can be flung back into the Roche lobe of the donor star [A. Langford et al. \(2022\)](#). In this way, V2400 Oph behaves in a somewhat similar way to the propeller system, AE Aqr, which is thought to expel material more energetically [G. A. Wynn et al. \(1997\)](#). Other IPs with an intact accretion stream (e.g. GK Per or DO Dra) that were previously observed by [P. E. Barrett et al. \(2017\)](#) remain undetected in the radio, despite being at a similar distance as V2400 Oph (700 pc). The way in which the WDs in V2400 Oph and AE Aqr interact with material from their donor stars may therefore drive the bright radio emission in these systems, which largely lacks the characteristic circular polarization seen from several other radio-bright CV systems.

[P. J. Meintjes & L. A. Venter \(2003\)](#) assume a similar interaction with blobs for AE Aqr. Using their values for electron  $\gamma$  (20) and magnetic field inside a blob ( $3 \text{ kG}$ )<sup>5</sup>, we obtain a synchrotron cooling time of

$$t = \frac{5.16 \times 10^8}{B^2\gamma} = 3 \text{ s}. \quad (2)$$

Lowering  $\gamma$  to  $\sim 1$  yields a cooling time of about a minute, which is similar to the minute-scale variation we see in Fig. 7. Since the spin period of the WD likely plays a role in the acceleration and V2400 Oph (927 s; [A. Langford et al. 2022](#)) has a much slower spin period than AE Aqr (33 s; [G. A. Wynn et al. 1997](#)), an electron population with a lower average energy would make sense. If we compare the light curve of V2400 Oph at 8–12 GHz with that at 2–4 GHz (Fig. 9), the shorter timescale in the former vs. the latter seems to correspond to predictions of the van der Laan model ([H. van der Laan 1966](#)), in which initially optically thick blobs expand. In this model, the expansion causes the frequency at which the material is optically thick to decrease, allowing for faster variation in the light curve at the higher frequencies that are optically thin.

<sup>5</sup> This estimate is the approximate surface magnetic field of the donor star. The magnetic field in a blob may be different.

Synchrotron emission is proposed to be responsible for the radio emission from AE Aqr (T. S. Bastian et al. 1988; P. E. Barrett 2022), but this is still debated (P. Jiang et al. 2024). Indeed, the sharp rise in the C-band SED, of spectral index  $\sim 0.7$ , presented in P. E. Barrett (2022) suggests the low frequency cutoff of a self-absorbed synchrotron spectrum (e.g. G. B. Rybicki & A. P. Lightman 1979). The X-band portion of the SED appears to decrease with an average spectral index of approximately  $-1$ . We see an even steeper (spectral index  $-2.2$  to  $-2.5$ ) spectral shape in V2400 Oph in X-band. We do not, however, observe the discontinuity shown in AE Aqr’s X-band SED by P. E. Barrett (2022), where the lower subband is spectrally flat at  $\sim 5.75 \mu\text{Jy}$  and the upper subband is also spectrally flat but  $\sim 5 \mu\text{Jy}$ . In K-band (though we note this was not taken simultaneously, P. E. Barrett (2022)), the flux continues to rise ( $\alpha \sim 2$ ), which matches the simulated spectrum for AE Aqr produced by blob shocking by P. J. Meintjes & L. A. Venter (2003). This spectrum was produced by simulating 10 blobs interacting with AE Aqr’s magnetosphere. The differences between the SEDs of V2400 Oph and AE Aqr may be explained by differences in the properties of each system, including the WD spin period and magnetic field strength.

While this discussion has mainly been focused on the long-term variation in V2400 Oph, it is not clear whether we can apply the same explanation to the short-term variation. On the one hand, the bright flare starting at 2:00 UTC on 2025 August 9 also has a steep spectral shape apparent in the dynamic SED (Fig. 9) that is comparable to the shape corresponding to the slow-varying component (see the peak centered on 2.5 GHz). We may, in this case, be able to explain it with synchrotron emission. However, variation of a similar timescale in S-band and X-band does not agree with our application of the van der Laan model above as we would expect the timescale to be longer in S-band. More confusing is the rapid variation in the 2025 August 15 data that at times is significantly circular polarized, and at other times is not. This behavior suggests that there are multiple emission mechanisms present in V2400 Oph, but it would be difficult to disentangle them. There may be one mechanism that produces circular polarization and one that does not or perhaps two circularly polarized sources of opposite handedness. Or perhaps a single mechanism which can either show circular polarization, or not.

Of the other sources that showed mildly variable or non-variable, broadband, radio emission without any flaring behavior or pronounced circular polarization, gyrosynchrotron emission by moderately relativistic electrons seems appropriate. Here we expect a flat spectrum, like what is shown in many of the SEDs in Section 3, and moderate levels of circular polarization, depending on the viewing angle G. A. Dulk (1985). For most observations, we do not have sufficient S/N ratio to identify measure the degree of circular polarization. However, for ST LMi on 2017 November 1 and V603 Aql on 2018 January 25, we can constrain the fractional circular polarization to  $\leq 30\%$ , which is consistent with gyrosynchrotron emission J. R. Callingham et al. (2024).

We compare the non-flaring luminosities of all targets except V2400 Oph in Table 7. These are presented alongside the spectral type of the donor, the mass accretion rate, and the magnetic field of the WD, allowing for identification of potential correlations. The accretion rate was chosen by first estimating whether it was in a high or low state using optical observations by the American Association of Variable Star Observers (AAVSO) and then searching for an estimate of the accretion rate in the literature that corresponded with that state. Among the polars, there is no clear correlation between the intrinsic luminosity and the other values presented. However, V603 Aql has a radio luminosity  $\sim 10\times$  brighter and a mass accretion rate  $\sim 100\times$  larger than the rest of the sample. We suggest that radio emission in V603 Aql may be related to its accretion and hence it would be a good candidate for testing the jet hypothesis for CVs.

## 5. CONCLUSIONS

We infer a general paradigm for the radio emission from most of the CVs we have studied here, with the notable exception of V2400 Oph. Outside of radio flares, these CVs are clearly detected in Stokes I with fluxes of 40–80  $\mu\text{Jy}$ , with circular polarization  $\lesssim 30\text{--}70\%$ . We tentatively attribute this persistent radio emission to gyrosynchrotron emission, due to their flat spectra and low levels of circular polarization. The flaring emission seen from EF Eri, ST LMi, and MR Ser (and possibly, at lower levels, from UZ For and ST LMi at 8–12 GHz), is much better described by a coherent plasma process such as plasma radiation or ECME. Due to the broadband features in their SEDs and fractional circular polarization of 79–96%, we can explain this emission either via plasma radiation, or from multiple regions (e.g. along a flux tube between the WD and donor star) that each produce ECME at their local electron gyrofrequencies. The steep radio spectrum and low circular polarization of V2400 Oph seem to indicate that synchrotron emission is responsible for its radio emission, but we note that the spectral index is exceptionally steep, meaning synchrotron may not be an appropriate explanation. The radio emission from V2400 Oph may be due to an interaction between blobs

of material orbiting the WD and the WD's strong magnetic field. The time scale on which we see variation in its radio light curve and spectral index is plausibly consistent with a simple expanding-blob model. The similarities between V2400 Oph and AE Aqr suggest that the emission source is common to both systems.

#### ACKNOWLEDGEMENTS

The authors would like to thank Gregg Hallinan for providing detailed discussions and feedback on the results of this work. This project was supported in part by an appointment to the NRC Research Associateship Program at the U.S. Naval Research Laboratory (NRL), administered by the Fellowships Office of the National Academies of Sciences, Engineering, and Medicine. Basic research at the NRL is supported by 6.1 Base funding. C. O. Heinke is supported by NSERC Discovery Grant RGPIN-2023-04264.

*Facilities:* VLA, AAVSO

*Software:* CASA (CASA Team et al. 2022), WSClean (A. R. Offringa et al. 2014), breizorro (A. J. Ramaila et al. 2023)

#### REFERENCES

- Bailer-Jones, C. A. L., Rybizki, J., Fouesneau, M., Demleitner, M., & Andrae, R. 2021, *The Astronomical Journal*, 161, 147, doi: [10.3847/1538-3881/abd806](https://doi.org/10.3847/1538-3881/abd806)
- Barrett, P., Dieck, C., Beasley, A. J., Mason, P. A., & Singh, K. P. 2020, *Advances in Space Research*, 66, 1226, doi: [10.1016/j.asr.2020.04.007](https://doi.org/10.1016/j.asr.2020.04.007)
- Barrett, P. E. 2022, *The Astronomical Journal*, 163, 58, doi: [10.3847/1538-3881/ac3ed9](https://doi.org/10.3847/1538-3881/ac3ed9)
- Barrett, P. E. priv. comm.
- Barrett, P. E., Dieck, C., Beasley, A. J., Singh, K. P., & Mason, P. A. 2017, *The Astronomical Journal*, 154, 252, doi: [10.3847/1538-3881/aa93ff](https://doi.org/10.3847/1538-3881/aa93ff)
- Bastian, T. S., Dulk, G. A., & Chanmugam, G. 1988, *ApJ*, 324, 431, doi: [10.1086/165906](https://doi.org/10.1086/165906)
- Beuermann, K., Euchner, F., Reinsch, K., Jordan, S., & Gänsicke, B. T. 2007, *A&A*, 463, 647, doi: [10.1051/0004-6361:20066332](https://doi.org/10.1051/0004-6361:20066332)
- Beuermann, K., Wheatley, P., Ramsay, G., Euchner, F., & Gänsicke, B. T. 2000, *A&A*, 354, L49, doi: [10.48550/arXiv.astro-ph/0001183](https://doi.org/10.48550/arXiv.astro-ph/0001183)
- Callingham, J. R., Pope, B. J. S., Kavanagh, R. D., et al. 2024, *Nature Astronomy*, 8, 1359, doi: [10.1038/s41550-024-02405-6](https://doi.org/10.1038/s41550-024-02405-6)
- CASA Team, Bean, B., Bhatnagar, S., et al. 2022, *Publications of the ASP*, 134, 114501, doi: [10.1088/1538-3873/ac9642](https://doi.org/10.1088/1538-3873/ac9642)
- Chanmugam, G., & Dulk, G. A. 1982, *ApJLetters*, 255, L107, doi: [10.1086/183779](https://doi.org/10.1086/183779)
- Coppejans, D. L., & Knigge, C. 2020, *NewAR*, 89, 101540, doi: [10.1016/j.newar.2020.101540](https://doi.org/10.1016/j.newar.2020.101540)
- Coppejans, D. L., Körding, E. G., Miller-Jones, J. C. A., et al. 2015, *MNRAS*, 451, 3801, doi: [10.1093/mnras/stv1225](https://doi.org/10.1093/mnras/stv1225)
- Dulk, G. A. 1985, *Annual Review of A&A*, 23, 169, doi: [10.1146/annurev.aa.23.090185.001125](https://doi.org/10.1146/annurev.aa.23.090185.001125)
- Dulk, G. A., Bastian, T. S., & Chanmugam, G. 1983, *ApJ*, 273, 249, doi: [10.1086/161363](https://doi.org/10.1086/161363)
- Ferrario, L., Bailey, J., & Wickramasinghe, D. T. 1993, *MNRAS*, 262, 285, doi: [10.1093/mnras/262.2.285](https://doi.org/10.1093/mnras/262.2.285)
- Hales, C. A. 2017, *CASA Interferometric Pipeline Polarization Calibration, Imaging Requirement, & Design Specifications*, NRAO
- Jiang, P., Cui, L., Liu, X., et al. 2024, *Monthly Notices of the Royal Astronomical Society*, 528, L112, doi: [10.1093/mnras/lsad178](https://doi.org/10.1093/mnras/lsad178)
- Khangale, Z. N., Potter, S. B., Woudt, P. A., et al. 2020, *MNRAS*, 492, 4298, doi: [10.1093/mnras/staa080](https://doi.org/10.1093/mnras/staa080)
- Langford, A., Littlefield, C., Garnavich, P., et al. 2022, *The Astronomical Journal*, 163, 4, doi: [10.3847/1538-3881/ac3010](https://doi.org/10.3847/1538-3881/ac3010)
- Lynden-Bell, D. 1996, *MNRAS*, 279, 389, doi: [10.1093/mnras/279.2.389](https://doi.org/10.1093/mnras/279.2.389)
- Meintjes, P. J., & Venter, L. A. 2003, *Monthly Notices of the Royal Astronomical Society*, 341, 891, doi: [10.1046/j.1365-8711.2003.06459.x](https://doi.org/10.1046/j.1365-8711.2003.06459.x)
- Offringa, A. R., McKinley, B., Hurley-Walker, et al. 2014, *MNRAS*, 444, 606, doi: [10.1093/mnras/stu1368](https://doi.org/10.1093/mnras/stu1368)
- Ramaila, A. J., Smirnov, O., & Heywood, I. 2023, *breizorro: Image masking tool*, *Astrophysics Source Code Library*, record ascl:2305.009 <http://ascl.net/2305.009>

- Ridder, M. E., Heinke, C. O., Sivakoff, G. R., & Hughes, A. K. 2023, *MNRAS*, 519, 5922, doi: [10.1093/mnras/stad038](https://doi.org/10.1093/mnras/stad038)
- Ridder, M. E., Hughes, A. K., Heinke, C. O., Sivakoff, G. R., & Sydora, R. D. 2025, *A&A*, 695, A96, doi: [10.1051/0004-6361/202452711](https://doi.org/10.1051/0004-6361/202452711)
- Ritter, H., & Kolb, U. 2003, *A&A*, 404, 301, doi: [10.1051/0004-6361:20030330](https://doi.org/10.1051/0004-6361:20030330)
- Rousseau, T., Fischer, A., Beuermann, K., & Woelk, U. 1996, *A&A*, 310, 526
- Rybicki, G. B., & Lightman, A. P. 1979, *Radiative processes in astrophysics* (Wiley)
- Sanad, M. R., & Bobrowsky, M. 2015, *New Astronomy*, 36, 110, doi: [10.1016/j.newast.2014.10.003](https://doi.org/10.1016/j.newast.2014.10.003)
- Schwöpe, A. D., Beuermann, K., Jordan, S., & Thomas, H. C. 1993, *A&A*, 278, 487
- Sion, E. M., Godon, P., & Bisol, A. 2015, *The Astronomical Journal*, 150, 36, doi: [10.1088/0004-6256/150/1/36](https://doi.org/10.1088/0004-6256/150/1/36)
- Suleymanov, V. F. 1992, *Soviet Astronomy Letters*, 18, 104
- van der Laan, H. 1966, *Nature*, 211, 1131, doi: [10.1038/2111131a0](https://doi.org/10.1038/2111131a0)
- Vedantham, H. K. 2021, *MNRAS*, 500, 3898, doi: [10.1093/mnras/staa3373](https://doi.org/10.1093/mnras/staa3373)
- Wynn, G. A., King, A. R., & Horne, K. 1997, *MNRAS*, 286, 436, doi: [10.1093/mnras/286.2.436](https://doi.org/10.1093/mnras/286.2.436)
- Yiu, T. W. H., Vedantham, H. K., Callingham, J. R., & Günther, M. N. 2024, *A&A*, 684, A3, doi: [10.1051/0004-6361/202347657](https://doi.org/10.1051/0004-6361/202347657)